Coastal Engineering 183 (2023) 104304

Contents lists available at ScienceDirect

Coastal Engineering

journal homepage: www.elsevier.com/locate/coastaleng

Coupled effects of wave and depth-dependent current interaction on loads on a bottom-fixed vertical slender cylinder☆

Zirui Xin [a], Xin Li [a,*], Yan Li [b,c,**]

[a] State Key Laboratory of Ocean Engineering, School of Naval Architecture, Ocean and Civil Engineering, Shanghai Jiao Tong University, Shanghai 200240, China
[b] Department of Mathematics, University of Bergen, N-5020 Bergen, Norway
[c] Department of Energy and Process Engineering, Norwegian University of Science and Technology, N-7491 Trondheim, Norway

ARTICLE INFO

Keywords:
Surface gravity waves
Wave and current interaction
Sheared current
Slender structures
Bottom-fixed cylinder
Offshore wind turbines

ABSTRACT

The coupled effects of waves and a subsurface current on the hydrodynamic loads on offshore slender structures in coastal water regions have been examined in this paper, especially the coupling of the weak nonlinearity of surface waves and the depth variation of a current profile. Based on a narrowband assumption, this paper firstly derives a novel semi-analytical framework which extends potential flow theory and the Direct Integration Method (DIM) proposed by Li and Ellingsen (2019), permitting the interaction between weakly nonlinear surface waves and an arbitrary depth-dependent subsurface current. This framework is numerically implemented, validated, and used to lead to the current-modified Morison equations which are used to analyze the loading on a bottom-fixed, vertically installed cylinder. We demonstrate the clear differences between the features of surface elevation and hydrodynamics loading exerted by the coupled interaction of irregular waves and a subsurface current in both operational and extreme sea states. Especially, we find that the occurrence probability of extremely large events represented by the statistical features of surface waves can be insignificant whereas the coupled effects of waves and current on the hydrodynamic loads are considerable, compared with the decoupled cases. This suggests that the conventional approach, which uses the statistical features of surface elevation to represent the extremely large wave events, and therefore risks posing to the safety of offshore structures, may not be sufficient when both the waves and a subsurface current are present and play a role in the hydrodynamic performances of offshore structures. Both the depth variation of a current profile and the direction between the wave propagation and current velocity are found to play an important role in the loads on offshore slender structures. A following and an opposing uniform current lead to overestimated and underestimated loads, respectively, compared to either a decoupled model or a coupled model with a more realistic representation of the current profile.

1. Introduction

Man-made structures installed in coastal water regions are widely exposed to realistic sea states where water waves, currents, and winds coexist. The realistic sea states can lead to the failure of structures as a result of their hydrodynamic loads and therefore, play a dominant role in both the cost, reliability, and safety of offshore structures, as is widely known. How to account for the effects of environmental conditions, especially due to waves and a current, in both an accurate and efficient manner have been a topic of practical importance in many applied fields. A few relevant examples are the design of slender structures used in the aquaculture (Shen et al., 2018; Faltinsen and Shen, 2018) and offshore wind sectors (Santo et al., 2018; Ghadirian et al., 2021), and the post-processing for *situ* measurements (Draycott et al., 2022). In this work, we focus on the coupled effects between surface waves and a background current on a bottom-fixed vertical slender cylinder.

Extremely large waves, known also as rogue or giant waves, have been a key driver in the design of offshore structures and safety operations at the sea. Many physical mechanisms are proposed for their formation (Onorato et al., 2013). For instance, the linear focusing of surface waves which can be a result of the refraction of surface waves by a varying bathymetry or current (White and Fornberg, 1998; Janssen

☆ X. Li acknowledges the support by the Major Science and Technology Projects of Hainan Province, China through project ZDKJ2019001; Y. Li is supported by the Research Council of Norway (RCN) through the FRIPRO mobility project 287389 and the POS-ERC 342480.
* Corresponding author.
** Corresponding author at: Department of Mathematics, University of Bergen, N-5020 Bergen, Norway.
E-mail addresses: lixin@sjtu.edu.cn (X. Li), yan.li@uib.no (Y. Li).

https://doi.org/10.1016/j.coastaleng.2023.104304
Received 26 December 2022; Received in revised form 16 March 2023; Accepted 3 April 2023
Available online 13 April 2023

and Herbers, 2009), modulational instability of deepwater waves in both presence and absence of an opposing current (Benjamin and Feir, 1967; Onorato et al., 2011), and nonlinear effects caused by waves experiencing inhomogeneous media, e.g., a varying depth (Trulsen et al., 2012; Zheng et al., 2020a; Trulsen et al., 2020; Li et al., 2021c,a,b) or current whose velocity profile has spatial variation (Shrira and Slunyaev, 2014b,a; Ardhuin et al., 2009; Ardhuin, 2017; Zheng et al., 2023; Zhang et al., 2022). Thereby, the interaction between waves and a background current is obviously relevant to the occurrence of rogue waves, posing a great risk to marine operations at the sea. Indeed, this point has been well supported by many examples of marine accidents which are the result of wave-current interaction; for instance, these that happened at Agulhas current (Dysthe et al., 2008), the mouth of Columbia River which has a long history of being littered with shipwrecks (Zippel and Thomson, 2017), Norwegian fjords (Saetra et al., 2021), and the South China Sea (Wang et al., 2014).

Although it has been well established that wave-and-current induced sea states, which may lead to a larger probability of rogue wave events, can pose severe risks to the safety at the sea, there is a need for clarifying how they affect the hydrodynamic loads on offshore structures with the main reason explained in the following. One key question that shall be addressed is whether the proxies to rogue wave events are sufficiently good to interpret the corresponding hydrodynamic loads on offshore structures. Statistical moments of the surface elevation are conventionally used as the proxies to rogue wave events with the amplitude and phase being the two main random variables (DNV–GL, 2014). In contrast, the hydrodynamic loads on offshore structures mostly rely on the flow kinematics (e.g., velocity and acceleration) despite that the kinematics and surface elevation have strong correlations. This difference cannot be disregarded when the statistics of surface waves and kinematics show obviously different features, as indicated in Trulsen et al. (2020), Lawrence et al. (2021) and Li et al. (2022). Therefore, it would be of practical significance if a direct connection of the wave–current interaction can be established with their hydrodynamic loads on offshore structures. To this end, the overall objective of this work is to study the coupled interaction effects of waves and a background current on offshore structures through relatively simple but sufficiently accurate approximations.

Physically, the coupling between waves and currents can be interpreted in a two-way manner; i.e. waves altering the properties of a current and *vice versa*. These of practical interests to engineering operations are primarily the former due to that a current has large temporal scales in variation (Quinn et al., 2017; Li and Ellingsen, 2019). The 'Doppler shift' is a widely known effect of current on waves, which refers to the wave number-weighted projection effect of the velocity of a uniform current on the direction of wave propagation (Peregrine, 1976). It leads to the different absolute frequencies of the waves with a fixed wave vector for the cases with a following and opposing uniform current. Mathematically, the underlying physics can be represented by a so-called 'Doppler shifted' term in the linear dispersion relation which is derived with the assumption of a uniform current in space. This assumption holds in the framework of potential flow theory which has been a key to wave–current-interaction-induced hydrodynamics. The hydrodynamic loads in sea states in the presence of waves and a current have been conventionally considered using potential wave theory; see, e.g. Shao and Faltinsen (2014), Shen et al. (2018), Faltinsen and Shen (2018), Zheng et al. (2020b), Yang et al. (2020), Ghadirian et al. (2021) and Qu et al. (2020). These works have examined wave–current induced loads on both fixed (Shen et al., 2018; Ghadirian et al., 2021) and floating slender structures (Shao and Faltinsen, 2014; Faltinsen and Shen, 2018; Qu et al., 2020; Zheng et al., 2020b; Yang et al., 2020).

Nevertheless, the current profile in nature is mostly non-uniform in space. This feature makes a striking difference because a spatially varying current can lead to rotational flow motions where the assumption of irrotationality no long holds (Shrira and Slunyaev, 2014b; Ellingsen, 2016). Thereby, the potential flow theory is inapplicable to the cases of waves atop a spatially varying current which gives rise to rotational flow motions. This makes it especially challenging to account for the wave–current interaction with semi-submerged structures using a more general framework than the potential flow theory. A very few exceptions are listed as follows. Chen and Basu (2018, 2019) have analyzed the wave–current interaction on the fatigue loads and global responses of structural motions of a spar-type floating wind turbine, respectively. Both find that the coupled effects between surface waves and a current are nontrivial, based on a linear theory for rotational flows.

Based on the discussion above, we have identified knowledge gaps in three aspects. Firstly, it is unclear whether the two proxies (skewness and kurtosis) to extreme wave events caused by the wave–current interaction can be directly used to elucidate loads on offshore structures. Secondly, there is a need for using a more general theoretical framework than the potential flow theory, which permits to account for the wave–current interaction effects on hydrodynamic loading of offshore structures in the cases with a varying current. Following the second aspect, how the wave nonlinearity plays a role is unclear, especially for offshore structures exposed to complex sea states due to surface waves coupled with a subsurface current. This paper sets out to fill in the knowledge gaps in the three aforementioned aspects. In contrast to a majority of works discussed which rely on the assumption of potential flow theory, this work will especially rely on a more general theory where fluid motions are permitted to be rotational as they indeed do in realistic circumstances. Compared with Chen and Basu (2018, 2019), this work will extend the analysis to allow for nonlinear waves with a focus on the hydrodynamic loads on offshore structures and a constructive comparison between properties of surface displacement of waves and direct hydrodynamic loading. To the best of the authors' knowledge, we believe this is for the first time that hydrodynamic loads on offshore structures arising from the coupling between nonlinear waves and an arbitrary depth-dependent current are examined.

This paper is organized as follows. The theoretical framework is firstly presented in Section 2, which explains how the sea states can be described using the more general Euler framework than the potential flow theory. The sea states take into account the physics up to the second order in wave steepness, corresponding to the lowest order of nonlinearity by virtue of simple and transparent illustration of the underlying physics. In Section 3, we present the details of the numerical implementation of the theory given in Section 2. In Section 4, the analysis of the loads in both extreme and operational conditions is carried out, where surface wave elevation is also examined. We draw conclusions from this paper in Section 5.

2. Theoretical framework

We consider a bottom fixed vertical circular cylinder with a radius, R, at a constant uniform depth, h. The cylinder is assumed to be a rigid body. A Cartesian coordinate system is chosen with the vertical axis z pointing upward. An undisturbed water surface is located at $z = 0$ and let $\mathbf{x} = (x, y)$ be the position vector in the horizontal plane, as shown in Fig. 1. The positive x axis is chosen such that it is in alignment with the main direction of wave propagation.

2.1. Description of the flow fields

In this section, we present the description of the flow fields in the absence of the cylinder. In other words, we consider a system of water region in the presence of surface waves in a background depth-dependent current. The velocity profile of the current is described by $\mathbf{U}_3 = (\mathbf{U}(z), 0)$, where $\mathbf{U} = (U_x(z), U_y(z))$ denotes the velocity vector in the horizontal plane with U_x and U_y denoting the components in the x and y directions, respectively. Due to the presence of the vertically sheared current, the potential flow theory is no longer applicable, as

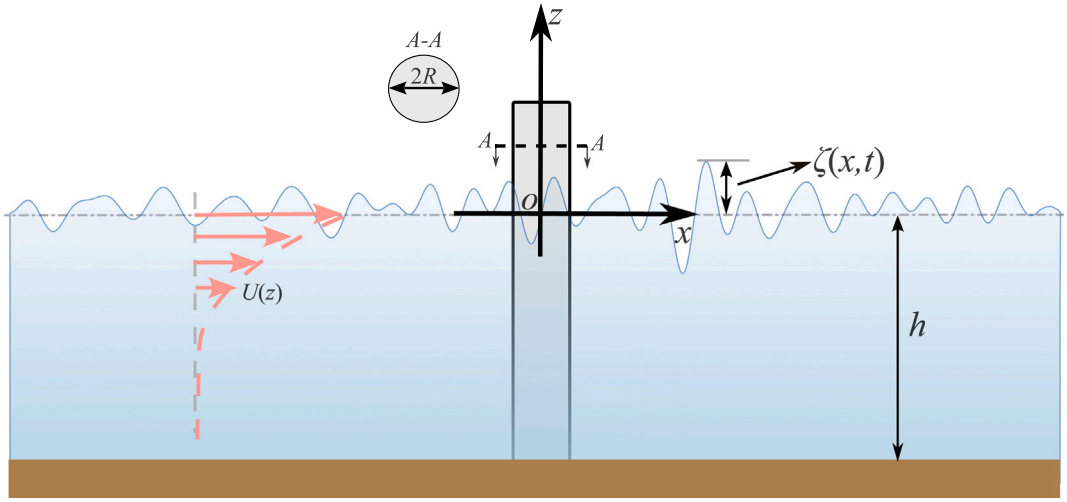

Fig. 1. Diagram of the system of a bottom-fixed vertical slender cylinder (with a radius, R) installed in a finite water region with a depth, h, where surface gravity waves and a tidal current coexist. The surface displacement in different sea states is given by $z = \zeta(\mathbf{x}, t)$ with $z = 0$ as the still water surface.

reported in a number of papers, e.g., Ellingsen (2016) and Li and Ellingsen (2016). Therefore, the velocity potential does not exist anymore. We consider effects of a current on waves but not *vice versa*, so that the incident waves are governed by the continuity and momentum equations for $-h < z < \zeta(\mathbf{x}, t)$:

$$\nabla_3 \cdot \mathbf{V} = 0, \tag{1}$$

$$\partial_t \mathbf{V} + (\mathbf{U}_3 \cdot \nabla_3)\mathbf{V} + (\mathbf{V} \cdot \nabla_3)\mathbf{U}_3 + \nabla_3 p = -(\mathbf{V} \cdot \nabla_3)\mathbf{V}, \tag{2}$$

where $\nabla_3 = [\nabla, \partial_z]$ denotes the gradient operator in three dimensions with $\nabla = [\partial_x, \partial_y]$ the gradient operator in the horizontal plane; $\mathbf{V}(\mathbf{x}, z, t) = [\mathbf{u}(\mathbf{x}, z, t), w(\mathbf{x}, z, t)]$ denotes the wave perturbed velocity, with $\mathbf{u} = [u(\mathbf{x}, z, t), v(\mathbf{x}, z, t)]$ and w as the velocity vector in the horizontal plane and the vertical velocity, respectively, and u and v as the velocity components in the x and y directions, respectively; ζ denotes the free surface elevation; $p(\mathbf{x}, z, t) = (P + \rho g z)/\rho$ denotes the dynamic pressure, with ρ, g, and $P(\mathbf{x}, z, t)$ as the fluid density, gravitational acceleration, and total pressure, respectively. The boundary conditions include the kinematic and dynamic conditions at the free water surface and a seabed condition. They are expressed as

$$p - g\zeta = 0 \text{ and } w = \partial_t \zeta + (\mathbf{U} + \mathbf{u}) \cdot \nabla \zeta \text{ for } z = \zeta, \tag{3}$$

$$w = 0 \text{ for } z = -h. \tag{4}$$

2.1.1. Construction of approximate solutions

We seek an approximate solution to the boundary value problem described by (1)–(4) based on a perturbation expansion and the narrow-band assumption of surface waves. Based on a perturbation expansion, the wave parameters are expressed in a form of power series in the dimensionless wave steepness $\epsilon = k_c A_c$, where k_c and A_c denote the wavenumber and amplitude of the characteristic wave, respectively, and kept up to the second order:

$$\mathbf{V} = \epsilon \mathbf{V}^{(1)}(\mathbf{x}, z, t) + \epsilon^2 \mathbf{V}^{(2)}(\mathbf{x}, z, t), \tag{5a}$$

$$p = \epsilon p^{(1)}(\mathbf{x}, z, t) + \epsilon^2 p^{(2)}(\mathbf{x}, z, t), \text{ and} \tag{5b}$$

$$\zeta = \epsilon \zeta^{(1)}(\mathbf{x}, t) + \epsilon^2 \zeta^{(2)}(\mathbf{x}, t), \tag{5c}$$

in which the superscript '(m)' denotes the mth order in wave steepness. For a train of linear irregular waves (random waves and wave groups), its elevation is given by

$$\zeta^{(1)} = \frac{1}{8\pi^2} \int_{-\infty}^{\infty} \left(|\hat{\zeta}(\mathbf{k})| e^{i\psi(\mathbf{k},\mathbf{x},t)} + \text{c.c.} \right) d\mathbf{k}, \tag{6}$$

where c.c. denotes the complex conjugates, $|\hat{\zeta}(\mathbf{k})|$ is the real wave amplitude of wave vector $\mathbf{k}$, and $\psi = \mathbf{k} \cdot \mathbf{x} - \omega t + \theta(\mathbf{k})$ denotes the wave phase with θ the initial phase of an individual monochromatic wave and ω denotes the angular frequency which obeys the linear dispersion relation, $\omega = \omega(\mathbf{k})$. We used the Direct Integral Method (DIM) proposed by Li and Ellingsen (2019) for the numerical solution of the linear dispersion relation. The DIM is also for the linear velocity fields, $\mathbf{u}^{(1)}$, $w^{(1)}$, and $p^{(1)}$. In the limiting cases where the current velocity is weak compared to the wave phase speed, a leading order approximation to the dispersion relation reads (Stewart and Joy, 1974; Ellingsen and Li, 2017)

$$\omega \approx \sqrt{g|\mathbf{k}| \tanh |\mathbf{k}|h} \left(1 + \varepsilon_U\right) \equiv \mathbf{k} \cdot \mathbf{U}_0 + \sqrt{g|\mathbf{k}| \tanh |\mathbf{k}|h} \left(1 - \delta_S\right), \tag{7a}$$

where $\mathbf{U}_0 \equiv \mathbf{U}(0)$ denotes the current velocity at the still water surface, $z = 0$, and ε_U and δ_S denote the current- and shear-modified correction to the dispersion relation, used in Kirby and Chen (1989) and Ellingsen and Li (2017), and given by, respectively

$$\varepsilon_U = \int_{-h}^{0} \frac{2\mathbf{k} \cdot \mathbf{U}(z)}{\sqrt{g|\mathbf{k}| \tanh |\mathbf{k}|h}} \frac{\cosh 2|\mathbf{k}|(z+h)}{\sinh 2|\mathbf{k}|h} |\mathbf{k}| dz, \tag{7b}$$

$$\delta_S = \int_{-h}^{0} \frac{\mathbf{k} \cdot \mathbf{U}'(z)}{\sqrt{g|\mathbf{k}| \tanh |\mathbf{k}|h}} \frac{\sinh 2|\mathbf{k}|(z+h)}{\sinh 2|\mathbf{k}|h} dz, \tag{7c}$$

where the prime denotes the derivative with respect to z (e.g., $\mathbf{U}' = \partial_z \mathbf{U}$ and $\mathbf{U}'' = \partial_{zz} \mathbf{U}$). It can be interpreted from (7a)–(7c) that the effects of current on the dispersion relation of waves are both depth and wavenumber weighted, meaning that the waves can only 'feel' the current profile and the profile shear in the water column from the surface down to half the wavelength. Hence, this depth-weighted property will affect the wave-induced kinematics, i.e., the velocity and acceleration of fluid particles. The linear velocity components and the pressure are obtained through an inverse Fourier transform as follows

$$\begin{bmatrix} \mathbf{u}^{(1)}(\mathbf{x}, z, t) \\ w^{(1)}(\mathbf{x}, z, t) \\ p^{(1)}(\mathbf{x}, z, t) \end{bmatrix} = \frac{1}{8\pi^2} \int_{-\infty}^{\infty} \begin{bmatrix} \hat{\mathbf{u}}^{(1)}(\mathbf{k}, z) \\ \hat{w}^{(1)}(\mathbf{k}, z) \\ \hat{p}^{(1)}(\mathbf{k}, z) \end{bmatrix} e^{i\psi(\mathbf{k},\mathbf{x},t)} d\mathbf{k} + \text{c.c.}, \tag{8}$$

in which the linear velocity $[\hat{\mathbf{u}}^{(1)}, \hat{w}^{(1)}]$ are obtained from the DIM.

Under the assumption of narrow-band waves which refers to the cases where the bandwidth of the spectrum of irregular waves is small compared with its spectral peak, we may obtain simplified approximations to the linear wave fields. Let $\mathbf{k}_0$ and $\omega_0 = \omega(\mathbf{k}_0)$ denote the wavenumber and frequency of the spectrum peak wave, respectively. We introduce δ to denote the dimensionless bandwidth. A narrow bandwidth implies $\delta = (\omega - \omega_0)/\omega_0 \ll 1$ for $\omega(\mathbf{k}) \neq 0$. Due to this assumption, the linear elevation, velocity, and pressure admit a slowly

varying envelope-type form (cf. e.g., §13 in Mei et al. (2005) and Li (2021)) as follows

$$\left[\zeta^{(1)}, \mathbf{V}^{(1)}, p^{(1)}\right] = \frac{1}{2}\left[A(\delta\mathbf{x}, \delta t), \bar{\mathbf{V}}(\delta\mathbf{x}, z, \delta t), \bar{p}(\delta\mathbf{x}, z, \delta t)\right] \mathrm{e}^{\mathrm{i}\psi_0} + \text{c.c.}, \tag{9}$$

where A, $\bar{\mathbf{V}}$, and $\bar{p}$ denote the envelope of linear elevation, velocity, pressure, respectively, with the superscript '(1)' eliminated for simplicity; $\psi_0 = \psi(\mathbf{k}_0, \mathbf{x}, t)$ denotes the wave phase of the peak wave.

2.1.2. Second-order waves

We will extend (Li and Ellingsen, 2019) in this work to allow for weakly nonlinear waves; i.e. second-order waves which admit the lowest order in nonlinearity but are crucial for fatigue life and extreme strength of offshore structures. The boundary value problem at the second order in wave steepness is obtained based on the following procedures in sequence. The continuity equation (1), and momentum equation (2), were firstly used to eliminate the horizontal velocity and pressure of the linear terms to produce an inviscid non-homogeneous Orr–Sommerfeld or Rayleigh equation governing the vertical velocity; the approximate solutions to the physical fields in a form of power series in wave steepness were then inserted to the Rayleigh equation where only the terms at the second order in wave steepness were kept; the kinematic and dynamic boundary conditions at the still water surface were used to produce a combined boundary condition at the still water surface, where the pressure and surface elevation of the linear terms were eliminated; the approximations to the physical fields were inserted to the combined boundary condition at the still water surface and the seabed boundary condition. Explicitly, the second-order boundary problem is given by

$$[(\partial_t + \mathbf{U}\cdot\nabla)\nabla_3^2 - \mathbf{U}''\cdot\nabla]w^{(2)} = \mathcal{R}(\mathbf{x}, z, t) \quad \text{for } -h \le z \le 0, \tag{10a}$$

$$[(\partial_t + \mathbf{U}\cdot\nabla)^2\partial_z - (\partial_t + \mathbf{U}\cdot\nabla)(\mathbf{U}'\cdot\nabla) - g\nabla^2]w^{(2)} = \mathcal{G}(\mathbf{x}, z, t) \quad \text{for } z = 0, \tag{10b}$$

$$w^{(2)} = 0 \text{ for } z = -h; \tag{10c}$$

where the non-vanishing forcing terms on the right hand side of (10a), (10b) are functions of the linear wave fields, written as

$$\mathcal{R} = \partial_z\nabla\cdot[(\mathbf{V}^{(1)}\cdot\nabla_3)\mathbf{u}^{(1)}] - \nabla^2[(\mathbf{V}^{(1)}\cdot\nabla_3)w^{(1)}], \tag{11a}$$

$$\mathcal{G} = [(\partial_t + \mathbf{U}\cdot\nabla)\nabla]\cdot[(\mathbf{V}^{(1)}\cdot\nabla_3)\mathbf{u}^{(1)}] - g\nabla^2[\nabla(\mathbf{u}^{(1)}\zeta^{(1)}) + \frac{1}{2}\mathbf{U}'\cdot\nabla(\zeta^{(1)})^2] - \nabla^2(\partial_t + \mathbf{U}\cdot\nabla)(\zeta^{(1)}\partial_z p^{(1)}). \tag{11b}$$

Expression (10a) is known as the (non-homogeneous) Rayleigh equation or the inviscid Orr–Sommerfeld equation. The boundary value problem described by (10a)–(10c) is in principle a second-order inhomogeneous partial differential equation with two boundary conditions, which can be directly solved numerically if an additional condition prescribed at a particular time instant is given. In this work, we used an additional condition of stationary sea states. Therefore, inserting the linear wave fields described by (9) into the second-order boundary value problem (10a), (10b), (10c) can lead to the second-order vertical velocity, $w^{(2)}$. The second-order wave surface elevation $\zeta^{(2)}$ can be obtained based on the following kinematic boundary condition

$$(\partial_t + \mathbf{U}\cdot\nabla)\zeta^{(2)} = w^{(2)} - \nabla\cdot(\zeta^{(1)}\mathbf{u}^{(1)}) - (\zeta^{(1)}\mathbf{U}')\cdot\nabla\zeta^{(1)}. \tag{12}$$

2.2. Modified Morison equation

The simplest description of the hydrodynamic loads on a bottom-fixed and vertical slender cylinder in various sea states is provided by the Morison equation (Morison, 1953), where the sea states are represented by the combinations of surface waves with and without a current. The Morison equation states the horizontal force per unit immersed length at a given depth can be given by

$$\mathrm{d}\mathbf{F} = \frac{\pi}{4}\rho D^2 C_m\dot{\mathbf{u}}_p + \frac{1}{2}\rho D C_d\mathbf{u}_p|\mathbf{u}_p|, \tag{13}$$

where C_m and C_d denote the inertial and drag coefficient, respectively; $\mathbf{u}_p$ and $\dot{\mathbf{u}}_p$ denote the horizontal orbital particle velocity and acceleration at the positions of the cylinder, respectively. It is understood that the flow wake regime, the roughness of the cylinder, Keulegan–Carpenter (KC) number, the Reynolds number, and relative dimension of the cylinder to the characteristic wave can affect the applicability of the Modified equation given by (13) and the values chosen for the coefficient of the inertial and drag force (see, e.g., Sumer and Fredse (2006), Sarpkaya (2004) and Ghadirian et al. (2021)). We argue that the modified Morison equation can provide a good approximation to the loads exerted on a smooth cylinder for all the load cases chosen in this work due to the regime of the dimensionless numbers explained as follows:

- $0.01 \lesssim D/\lambda_p \lesssim 0.04$ with $D = 2R$ as the diameter of the cylinder and λ_p as the wavelength of a spectral peak wave. This suggests that the diffraction effects of waves are negligible;
- $3 \lesssim KC \lesssim 8$, where $KC = U_r T_p/D$ with U_r and T_p as the characteristic relative particle velocity and the period of a spectral peak wave, respectively.
- $\mathrm{Re} = U_r D/\nu \sim 10^6$ with ν as the kinematic viscosity coefficient.

Following Bredmose and Pegalajar-Jurado (2021) and Ghadirian et al. (2021), the choice of $C_m \approx 2$ and $C_d \approx 1$ was made due to the similarity in the regime of the dimensionless numbers and environmental conditions. It should be noted that, due to the steady flow (i.e., represented by the non-vanishing current $\mathbf{U}(z)$) and its profile shear, additional loads arising from the Vortex-Induced Vibrations (VIVs) can be exerted, see, Sarpkaya (2004) and references therein for details. As the focus of this paper is on the current-modified wave kinematics, we may neglect the effects of VIVs due to a steady flow alone.

For a bottom-fixed cylinder, we may further neglect its displacements as they are small compared to the particle motions of the fluid. Therefore, the particle horizontal velocity and acceleration at the cylinder positions are given by, respectively

$$\mathbf{u}_p = \mathbf{u} + \mathbf{U} \text{ and} \tag{14a}$$

$$\dot{\mathbf{u}}_p = \partial_t(\mathbf{u} + \mathbf{U}) + \left[(\mathbf{V} + \mathbf{U}_3)\cdot\nabla_3\right](\mathbf{u} + \mathbf{U}), \tag{14b}$$

where the sea states with waves or current only means that $\mathbf{U}$ or $\mathbf{u}$ vanishes, respectively. As we aim to examine the coupled effects of the interaction between waves and a current, it would be necessary to clarify the forces which neglect their coupling. To this end, we introduce the force due to waves or currents only

$$\mathrm{d}\mathbf{F}_{\mathrm{nc}} = \frac{\pi}{4}\rho D^2 C_m[\partial_t\mathbf{u}_{\mathrm{nc}} + (\mathbf{V}_{\mathrm{nc}}\cdot\nabla_3)\mathbf{u}_{\mathrm{nc}}] + \frac{1}{2}\rho D C_d\mathbf{u}_{\mathrm{nc}}|\mathbf{u}_{\mathrm{nc}}|, \text{ and} \tag{15a}$$

$$\mathrm{d}\mathbf{F}_c = \frac{\pi}{4}\rho D^2 C_m[\partial_t\mathbf{U} + (\mathbf{U}_3\cdot\nabla_3)\mathbf{U}] + \frac{1}{2}\rho D C_d\mathbf{U}|\mathbf{U}|, \tag{15b}$$

where the subscripts 'nc' and 'c' denotes waves without current and current only, respectively. In the limiting cases of waves with a vanishing current, the wave-induced velocity follows the classic second-order theory for narrow-band surface waves as explained in § 13 in Mei et al. (2005). Otherwise, the wave-induced velocity, $\mathbf{u} \approx \mathbf{u}^{(1)} + \mathbf{u}^{(2)}$, depends on the profile of the current as explained in Section 2. A second-order approximation, $\mathbf{V} \approx \mathbf{V}^{(1)} + \mathbf{V}^{(2)}$ to the wave-induced velocity is used for the hydrodynamic forces per unit depth.

The total horizontal force is a result of the integration of the force per unit depth over the entire water column from the seabed to the free water surface and the total moment is especially estimated with the center at the mudline of the cylinder, given by, respectively,

$$\mathbf{F} = \int_{-h}^{\zeta}\mathrm{d}\mathbf{F}, \text{ yielding } \mathbf{F} \approx \int_{-h}^{0}\mathrm{d}\mathbf{F} + \left[(\zeta^{(1)} + \zeta^{(2)})\mathrm{d}\mathbf{F}_0\right], \tag{16a}$$

$$\mathbf{M} = \int_{-h}^{\zeta}(z+h)\mathrm{d}\mathbf{F}, \text{ leading to } \mathbf{M} \approx \int_{-h}^{0}(z+h)\mathrm{d}\mathbf{F} + \frac{1}{2}\left[(\zeta^{(1)} + \zeta^{(2)})(\zeta^{(1)} + \zeta^{(2)} + 2h)\mathrm{d}\mathbf{F}_0\right], \tag{16b}$$

where $d\mathbf{F}_0$ denotes the force per unit length measured at the still water surface, $z = 0$. We will repeatedly refer to (16a) and (16b) in Section 4 for the analysis based on numerical simulations.

3. Numerical implementation

The numerical implementation of the theory presented in Section 2 has been carried out for different sea states in two dimensions. The customized scripts used for the numerical simulations are validated in Appendix A where the validation includes the comparisons with available laboratory measurements for the cases of weakly nonlinear waves in an arbitrarily depth-varying current and a comparison with theoretical results in the limiting cases of a nonlinear focus wave group in the absence of a current. In this section, we focus on the realization of irregular waves in Section 3.1, the definition of a current profile in Section 3.2, cases matrix in Section 3.3 and the coupled and decoupled models in Section 3.4.

3.1. Realization of irregular waves

A train of irregular waves is generated from a power energy spectrum in frequency, $S(\omega)$, with the surface elevation due to linear waves given by

$$\zeta^{(1)}(\mathbf{x}, t) = \sum_{n=1}^{N} a_n \cos(k_n x - \omega_n t + \theta_n), \tag{17}$$

where N denotes the number of wave components considered, a_n, k_n, ω_n, and θ_n denote the amplitude, wavenumber, angular frequency, and phase of the nth wave. With a given frequency, the dispersion relation $\omega_n = \omega(k_n)$ is solved numerically for wavenumber, k_n, using the DIM method by Li and Ellingsen (2019) as noted. We will examine both fatigue and extreme loads. The former relies on the realizations of random waves and the latter on focus wave groups for the design in a deterministic perspective. Hence, it is required to realize the trains of both random waves and focus wave groups, which can be obtained by using different approaches for the wave amplitudes and phases with a fixed power energy spectrum, $S(\omega)$.

We start with the realization of a train of *random waves*. It is based on the assumption of the randomness in two independent variables which include the random amplitude, $\tilde{a}$, and phase, $\tilde{\theta}$. Following Tayfun (1980) and Tucker et al. (1984), we assume the probability density function for the random amplitude follows the Rayleigh distribution and the random phase follows a uniform distribution in the range from 0 to 2π. As has been well understood, the parameters for the Rayleigh distribution were chosen from a fixed power spectrum such that the variance of the Rayleigh distribution equals the zeroth moment, m_0, of the power energy spectrum. This especially means the significant wave height, H_s, of a realized time record of the randomized linear surface elevation should admit $H_s = 4\sqrt{m_0}$. Mathematically, the surface elevation due to a train of random waves also has an explicit form similar to (17) with $a_n \to \tilde{a}$ and $\theta_n \to \tilde{\theta}$. For the statistical convergence, we used at least 40 realizations of random waves, with around 500 wave periods per realization per case. The convergence of the skewness and kurtosis is especially ascertained.

In contrast, *focus wave groups* are represented with the introduction of the amplitude, A_f, location, x_f, time t_f, and phase, θ_f, for a wave group at linear focus. Therefore, we obtain (see, e.g., Li and Li (2021))

$$a_n = \frac{A_f}{A_s}\sqrt{2S(\omega_n)\Delta\omega_n} \text{ and } \theta_n = \theta_f - k_n x_f + \omega_n t_f, \text{ with}$$
$$A_s = \sum_{n=1}^{N} \sqrt{2S(\omega_n)\Delta\omega_n}, \tag{18}$$

which suggests that for the wave group at linear focus, $\zeta^{(1)}(x_f, t_f) = A_f \cos(\theta_f)$ is admitted. In all relevant cases examined in Section 4, we used $\theta_f = 0$, meaning that the wave group focuses at the wave crest, and the amplitude at linear focus is prescribed using $A_f = 2\sqrt{m_0} \equiv H_s/2$.

Table 1
Parameters chosen for the velocity profile of different currents, where $\max(|U(z)|)/c_{gp,0} \le 0.15$ with $c_{gp,0}$ the group velocity of the spectral peak wave. The parameters α, β, γ, and $U(0)$ are based on (19). 'F.', 'O', 'P.', 'N.', 'S', and 'C' stand for following, opposing, positive, negative, surface shear, and current, respectively.

Case No.	Name	α	β	γ	$U(0)$ [m/s]
C0	'Decoupled'	–	–	–	0
C1	'F. uniform'	–	0	1	1.75
C2	'O. uniform'	–	0	−1	−1.75
C3	'F.C., N.S.'	4	−1	1	0
C4	'O.C., P.S.'	4	1	−1	0
C5	'F.C., P.S.'	4	1	0	1.75
C6	'O.C., N.S.'	4	−1	0	−1.75

Table 2
Parameters for extreme wave events typical of the South China sea.

Case name	$k_{p,0}$ [m^{-1}]	$k_{p,0}h$	T_p [s]	H_s [m]	f_p [Hz]	$\epsilon = k_{p,0}H_s/2$
10y	0.033	1.00	12.66	8.00	0.079	0.13
20y	0.033	1.00	12.66	10.00	0.079	0.17
50y	0.033	1.00	12.66	11.00	0.079	0.18
100y	0.033	1.00	12.66	13.00	0.079	0.21

3.2. Velocity profile of current

In order to consider different sea states where both waves and a current are present, a prescribed velocity profile of current has been assumed and given by

$$U(z) = \left[\beta \exp(\alpha k_c z) + \gamma\right] U_c, \tag{19}$$

where α, β, and γ denote the dimensionless parameters which vary for different realistic sea states, and k_c and U_c ($U_c \ge 0$) denote the characteristic wavenumber and velocity, respectively. With different values chosen for the dimensionless parameters, the velocity profiles are grouped into the scenarios as listed below.

- No current: $U_c = 0$. With varying parameters for waves, this case also corresponds to a decoupled model as it physically means the waves (current) do not 'feel' the presence of current (waves) and the current, despite nonvanishing, is 'felt' as if $U = 0$ by the waves.
- Following (or opposing) uniform current: $\beta = 0$, $\gamma = 1$ (or $\gamma = -1$), and $U_c \neq 0$; therefore, $U(z) = U_c > 0$ (or $U(z) = -U_c < 0$). A uniform current can also be interpreted as a current whose velocity profile has zero surface shear, i.e., at $z = 0$, and throughout the water column.
- A following (opposing) current with positive (negative) shear at the still water surface: $(\beta + \gamma) > 0$ (or $(\beta + \gamma) < 0$), $\alpha\beta > 0$ (or $\alpha\beta < 0$), and $U_c \neq 0$.
- A following (opposing) current with negative (positive) shear at the still water surface: $(\beta + \gamma) > 0$ (or $(\beta + \gamma) < 0$), $\alpha\beta < 0$ (or $\alpha\beta > 0$), and $U_c \neq 0$.

Due to the cases listed, seven typical velocity profiles of current are used with the values chosen for the parameters shown in Table 1 and the velocity $U(z)$ at different depths (z) shown in Fig. 2. These profiles can lead to different combinations of sea states with the additional presence of waves, as explained in Section 4.

3.3. Cases matrix

To avoid the ambiguity likely caused by that the linear dispersion relation of surface waves varies with the velocity profile of a current, we define the one in decoupled cases where the wavelength (wave number) and frequency (period) are independent of a current profile; explicitly

$$\omega_p^2 = g k_{p,0} \tanh k_{p,0} h, \tag{20}$$

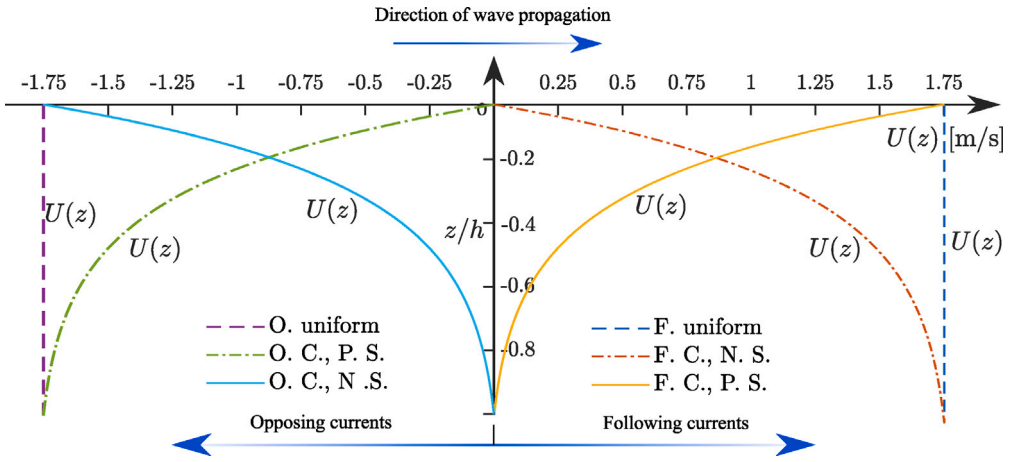

Fig. 2. Velocity profiles of horizontally-oriented and depth-dependent current, $U(z)$.

Table 3
Parameters for wave events with a varying wave period of the peak wave states in random seas. The highlighted case, W5, is used but with a varying significant wave height for examining the effects of significant wave height.

Case name	$k_{p,0}$ [m^{-1}]	$k_{p,0}h$	T_p [s]	H_s [m]	f [Hz]	$\epsilon = k_{p,0}H_s/2$
W1	0.057	1.71	8.70	6.2	0.115	0.18
W2	0.048	1.44	9.70	6.2	0.103	0.15
W3	0.042	1.25	10.70	6.2	0.093	0.13
W4	0.037	1.10	11.70	6.2	0.085	0.11
W5	0.033	0.99	12.70	6.2	0.079	0.10
W6	0.030	0.90	13.70	6.2	0.073	0.09
W7	0.028	0.83	14.70	6.2	0.068	0.09
W8	0.025	0.76	15.70	6.2	0.064	0.08
W9	0.024	0.71	16.70	6.2	0.060	0.07
W10	0.022	0.66	17.70	6.2	0.056	0.07

where ω_p and $k_{p,0}$ denote the angular frequency and wavenumber of the peak wave of a spectrum. The wavelength, $\lambda_{p,0} = 2\pi/k_{p,0}$, frequency $f_p = \omega_p/(2\pi)$, and period $T_p = 1/f_p$ of the spectral peak wave in a decoupled model are also used as the main scaling parameters.

The cases chosen for wave parameters are shown in Tables 2 and 3, which are independent of a current profile. Tables 2 and 3 correspond to extreme wave cases and operational cases with a varying peak period of a spectral peak wave, respectively.

3.4. Coupled and decoupled models

As mentioned, one of our main objectives is to examine the coupled effects of waves and currents. This is achieved through the comparisons of results between decoupled and coupled models. Both the linear dispersion relation governing the wave properties and the wave-induced fields can be current modified. Especially for a fixed frequency in a coupled model, the wavenumber varies with the current profile. Therefore, with a fixed prescribed power energy spectrum, $S(\omega_i)$, which is numerically implemented for the realization of irregular waves as explained in Section 3.1, an individual wave component with a specific angular frequency has an amplitude and wavenumber that are independent and dependent of a current profile in coupled models, respectively. In a decoupled model, the amplitude and wavenumber will not 'feel' the additional presence of current. Moreover, the decoupled models also mean that the horizontal force and moment can be simply obtained from the linear superposition of the results for cases with waves and currents only; explicitly,

$$\mathbf{F} = \mathbf{F}_{nc} + \mathbf{F}_c \quad \text{and} \quad \mathbf{M} = \mathbf{M}_{nc} + \mathbf{M}_c. \tag{21}$$

It is understood that the coupling is dominant by the current modified properties of surface waves. It means that the differences between the coupled and decoupled models are reflected in the wave-induced terms which are affected by a current in the coupled models. For better comparisons presented in Section 4, we chose to show the (current-modified) wave-induced loads only, namely $\mathbf{F}-\mathbf{F}_c$ and $\mathbf{M}-\mathbf{M}_c$ in coupled models and $\mathbf{F}_{nc}$ and $\mathbf{M}_{nc}$ in decoupled models. Doing so allows us to carry out the analysis of cases with the same waves but different current profiles together, and especially this will not affect the conclusions drawn from this paper.

4. Results and analysis

In this section, we examine both the loads in extreme environmental conditions (Section 4.1) and fatigue loads (Section 4.2) based on the numerical simulations following Section 3, especially Section 3.4 for the comparisons between the decoupled and coupled models in two dimensions.

4.1. Loads in extreme environmental events

The analysis of the loads on a bottom fixed and vertical slender cylinder is computed under extreme environmental conditions with the assumption of a rigid body. To this end, two classic approaches can be used (DNV–GL, 2014), which are the approach based on a 'design' wave in the deterministic perspective and a stochastic approach for statistical behavior of responses. Both approaches are used in this work with the former and latter presented in Sections 4.1.1 and 4.1.2, respectively.

4.1.1. Focus wave group

We used a wave group – which linearly focuses at a prescribed location ($x_f/\lambda_{p,0} = 0$) and time ($t_f/T_p = 0$) with a given amplitude, $A_f = 2\sqrt{m_0} \equiv H_s/2$ as noted – as our 'design' wave; see, e.g., Whittaker et al. (2016) and Feng et al. (2020) where similar setups are used. Using the case '50y' presented in Table 2 for the realization of random waves, we examine the hydrodynamic force and moment and surface elevation shown in Fig. 3 with different velocity profiles of current. The current profile is given by (19) with the specific values chosen for the parameters shown in Table 1. The configuration of the different environmental conditions has the physical implications as follows. The linear elevation of the focus wave group has the same linear temporal distribution regardless of a background current but varies differently in space as a result of the effect of different current profiles on the wavenumber due to the current-modified dispersion relation. The second-order correction to the surface elevation will differ both spatially and temporally since a current profile can in addition play a role in the amplitude of the second-order waves, as shown in Section 2.1.2. As a result, the coupled effects between surface waves and a current will lead to different kinematics (e.g., velocity and acceleration

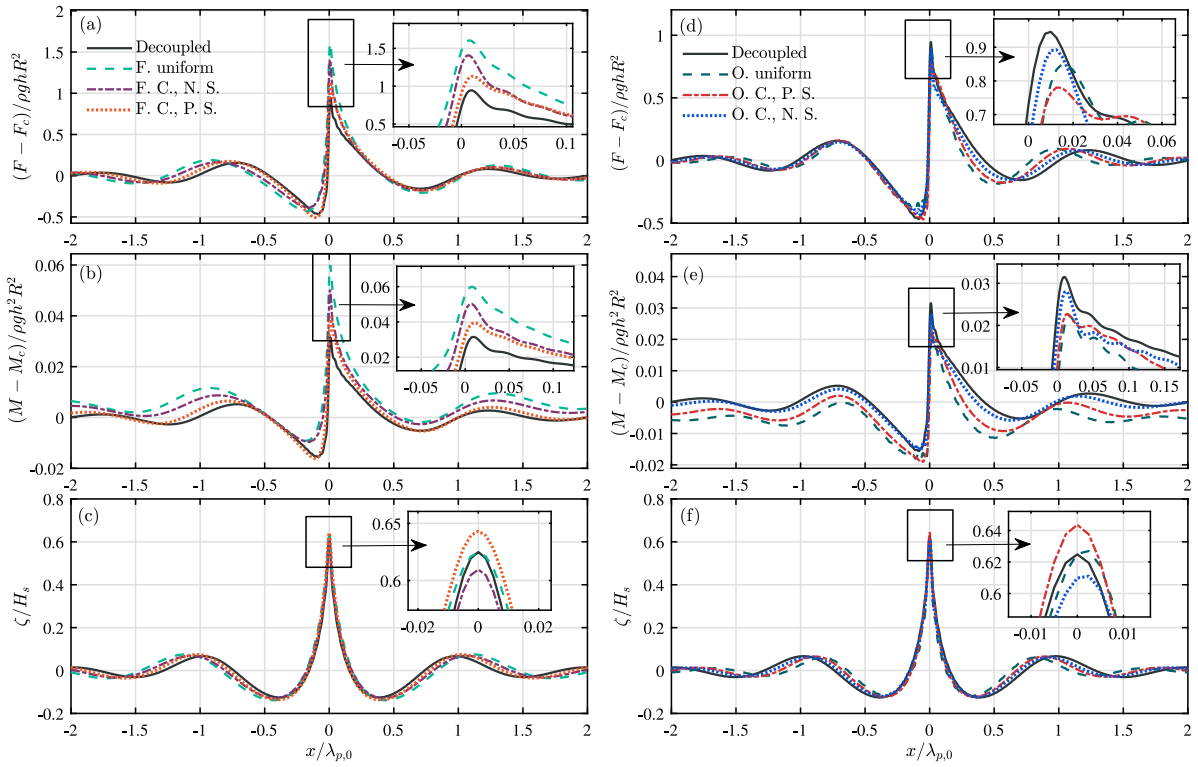

Fig. 3. Spatial distribution of the horizontal force (panels a, d) and moment (panels b, e) relative to the case with current only and surface elevation (panels c and f) due to a focus wave group at the time instant where the group focuses linearly, $t = t_f$, for which case '50y' was used for wave parameters with 6 different velocity profiles shown in Table 1.

of water particles) and therefore, the hydrodynamic force and moment on the cylinder. As noted, for the coupled effects of waves and a current on hydrodynamic loading on the cylinder, we use the decoupled cases as our reference and compare them with the associated coupled cases. In particular, the loads on the cylinder due to current only are removed in the loads shown in Fig. 3, following the explanation in Section 3.4.

We see from Fig. 3 that the coupled effects on both surface elevation and the loads on the cylinder play an important role in both the magnitude and the spatial distribution, as reflected by the obvious differences between the coupled and decoupled cases. Focusing on the loads in Fig. 3 (the panels in the top two rows), it can be clearly seen that the coupling of waves with a following (opposing) current leads to an increased (declined) maximum near the focus position ($x_f = 0$) at the time instant $t = t_f$, compared with the decoupled case. Nevertheless, it is not so for the maximum of the surface elevation shown in Fig. 3(c, f) where the maximum depends on both the direction of the current profile to waves and the sign of the profile shear at the still water surface. The extent to which the maximum loads can be increased/decreased depends on the realistic current profile. In the coupled cases, a different current profile can lead to significant differences in the horizontal force, $F - F_c$. To be more specific, compared with the decoupled case, the three cases with a following current show a difference by ~25%, ~50%, ~65% for the case with a current profile which has positive ('F.C., P.S.'), negative ('F.C., N.S.'), and zero (i.e., a uniform current, 'F. uniform') surface shear, respectively, whereas the differences of $M - M_c$ are by ~33%, ~66%, and ~100%, respectively. In contrast, the maximum differences for the maximum of the surface elevation between the coupled and decoupled cases are less than 4%, showing that the coupled effects on surface elevation are much minor compared to their effects on the loads. We see that the location of the crest maximum of the surface elevation does not coincide with that of the horizontal forces. This may be likely due to a phase shift between the surface elevation and horizontal force or moment. The difference in the location suggests that the main features of the surface elevation are not necessarily good representations to the extreme loads on offshore structures, in agreement with Trulsen et al. (2020) which have highlighted the differences of the features of wave kinematics from these of the surface elevation in the design of offshore structures.

4.1.2. The averaging of the largest wave groups

For the extreme conditions in the statistical analysis, we examine the averaging of the largest wave groups following Tang and Adcock (2021). The averaging is carried out through the following sequential procedures by choosing the groups containing an extremely large crest. Firstly, we pick out all crests in a sufficiently long spatial record and rank them and identify the locations of the top N_c largest crests, with N_c denoting the number of crests chosen. We next align the locations of all chosen crests and add them up together with their adjacent neighbors within a distance of $3 \times \lambda_{p,0}$. The final step is the averaging, i.e., dividing the resulting group after the linear superposition by N_c. Explicitly, the averaging operator is given by

$$\bar{\chi}(X) = \frac{1}{N_c}\sum_{j=1}^{N_c}\chi(X) \text{ with } X = x - x_{j,c} \text{ and } -3\lambda_{p,0} \le X \le 3\lambda_{p,0}, \qquad (22)$$

where χ denotes an arbitrary parameter chosen which can be the surface elevation, the horizontal force, $F - F_c$, or moment, $M - M_c$; $x_{j,c}$ denotes the location of the top jth largest crest; and $X/\lambda_{p,0} = 0$ is the location of the averaging of the largest crests. Due to the location alignment chosen for the averaging, the location difference of the maximum of the surface elevation from the hydrodynamics loads, as shown in Fig. 3, has been removed by choice, and therefore cannot be reflected in the analysis.

Fig. 4 shows the averaged largest group of the horizontal force, $\overline{F - F_c}$, moment, $\overline{M - M_c}$, and surface elevation, with $N_c = 100$ chosen. It should be noted that $\zeta_c = 0$ is admitted which means the current only is assumed to lead to a negligible surface elevation. The coupled effects of waves and a current with different profiles on the force, moment, and surface elevation in Fig. 4 show qualitatively similar observations

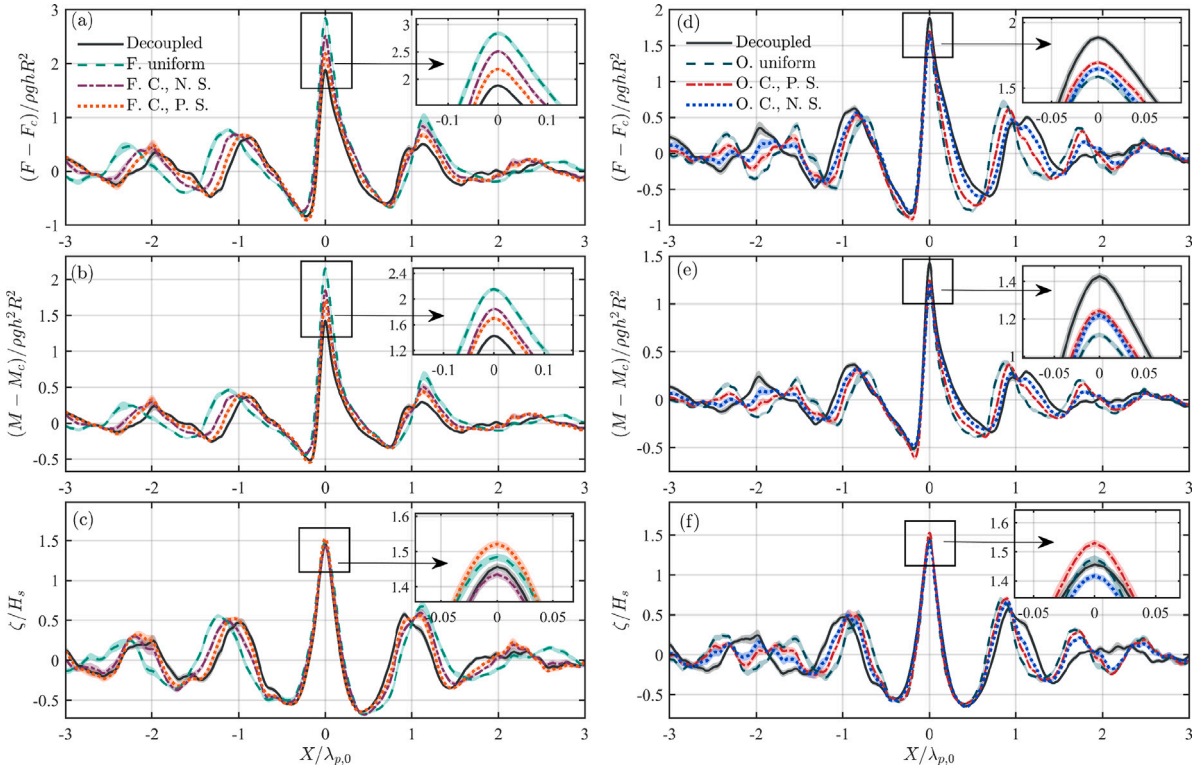

Fig. 4. The averaging of the top N_c ($N_c = 100$) largest crests of the horizontal force, $\overline{F-F_c}$, (panels a and d), moment, $\overline{M-M_c}$ (panels b and e), and surface elevation (panels c and f).

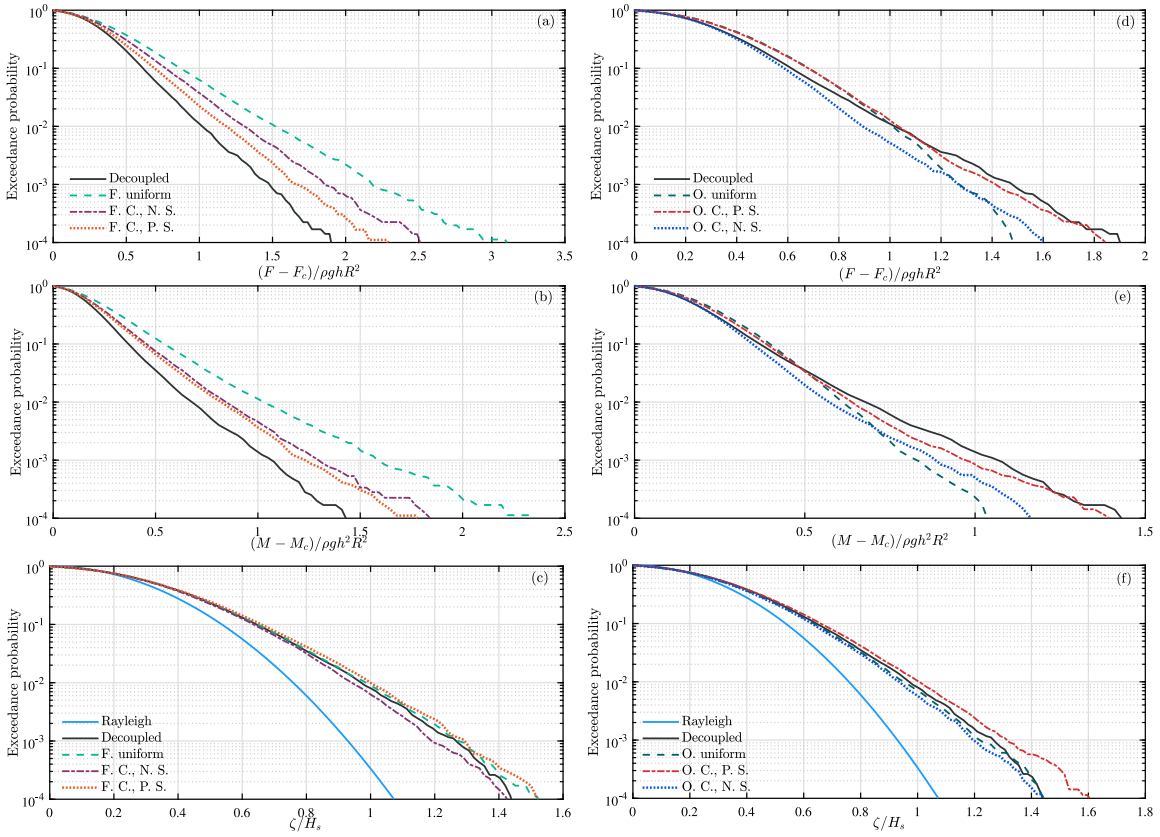

Fig. 5. Exceedance probability of the crests of horizontal force (panels a and d), moment (panels b and e), surface elevation (panels c and f).

as Fig. 3 as it should due to the consistent underlying physics. Compared with the decoupled model, the coupled effects with a following (opposing) current lead to an increased (decreased) maximum crest of both the force and moment. The extent to which the coupled effects are on the force and moment depends on the realistic profile of a current. As shown in Fig. 4 for the cases with a following current, the coupled effects on both the force and moment in descending quantitative order are the cases where a current profile has zero, negative, and positive surface shear. They show different quantitative effects for the cases with an opposing current. It is ranked from a current with a positive, negative, and zero (i.e., uniform current) surface shear in descending order. This suggests that an accurate description of a background current plays an extremely important role in the extremes of hydrodynamic loads on the slender cylinder examined. In realistic waters, currents are often not uniform, and using a depth uniform model will lead to too conserved and underestimated extreme loads for waves with a following and opposing current, respectively. The former can lead to an overestimate of loads by ∼20% compared to the case with a more realistic current profile (e.g., the following current with negative surface shear).

In contrast, Fig. 4 shows that the coupled effects of waves and varying currents on the maximum crest of the surface elevation depend on both the velocity direction of current to waves and realistic profile (or the sign of the profile shear at the still water surface), making a difference by $\lesssim$5%.

4.1.3. Exceedance probability of crest

The exceedance probability of the crests of horizontal force, moment, and elevation is shown in Fig. 5. Specifically, the exceedance probability refers to the occurrence probability of the event where a random variable of interests is larger than a specific value. We see clearly from Fig. 5 that, compared with the decoupled case, the probability of the larger crest events of loads corresponding to these at the high-value end, is much larger and relatively smaller for the case with a following and opposing current, respectively. This mainly arises from the coupled effects of waves and a current. In particular, the case with a following uniform current leads to the largest exceedance probability for a particular event to occur, compared with other cases with and without a current (the decoupled model). This is shown by the exceedance probability at a particular value for the horizontal axis in the cases with a different current profile. The crest load which appears once every 1000 events, i.e., where the exceedance probability is 10^{-3}, is larger than that in the decoupled case by 7%, 25%, and 50% for the case with a following current with positive, negative, and zero surface shear (uniform current), respectively. The coupled effects on the exceedance crest probability of surface displacement are minor, similar to cases examined in Section 4.1.1 and Section 4.1.2, compared with the decoupled cases.

4.2. Fatigue loads

The fatigue loads can be examined through the statistical moments of a sufficiently long record from the realizations of horizontal force, moment, and surface elevation. The statistical moments examined here include the mean m, standard deviation, σ, skewness, s, and kurtosis, κ, defined as, respectively

$$m = \langle \chi \rangle,\ \sigma = \sqrt{\langle (\chi - m)^2 \rangle},\ \ s = \frac{\langle (\chi - m)^3 \rangle}{\sigma^3},\ \kappa = \frac{\langle (\chi - m)^4 \rangle}{\sigma^4}, \tag{23}$$

where χ denotes an arbitrary random variable and $\langle \cdots \rangle$ denotes the expected value of a random variable.

4.2.1. Statistical moments against a varying significant wave height

The statistical moments varying with significant wave height, H_s, are shown in Fig. 6. It can be seen from Fig. 6 that they vary with the significant height in a monotonic manner for the horizontal force, moment, and surface elevation. As the significant height increases, the statistical moments of the hydrodynamic loads increase nonlinearly but these of the surface elevation grow more linearly except for the kurtosis. This suggests that the main contribution of the hydrodynamic forces to the statistical moments are both linear and nonlinear waves whereas the dominant contribution of surface elevation comes primarily from the linear components.

Consistent with the observations analyzed in Section 4.1, Fig. 6 shows that the coupled effects of waves and a current are much stronger on the hydrodynamic loads compared to the surface elevation. The coupling of cases with a following current especially leads to more increased statistical moments as the significant wave height increases, compared to the decoupled model. Thereby, it can be inferred that the coupled interaction for waves with a following current may result in larger fatigue loads as reflected by the standard deviation of both the horizontal force and moment.

As shown in Fig. 6, the coupled effects are stronger on the two proxies (i.e., skewness and kurtosis) to the extremely large events, compared with these on the standard deviation which is a good physical interpretation of fatigue loads. The results are consistent with the analysis of extreme environmental events presented in Section 4.1.

4.2.2. Statistical moments against a varying period of spectral peak wave

The statistical moments varying with the period of spectral peak wave, T_p, are shown in Fig. 7 based on the definition given by (23). The cases examined are presented in Table 3, meaning that the wavenumber and angular frequency of the spectral peak wave vary with the period T_p whereas both the velocity profile and the significant wave height (therefore, the zeroth moment of the power energy spectrum prescribed) are fixed. For a given wave period, T_p, in the cases with a following current, it is shown in Fig. 7 that the standard deviation, skewness, and kurtosis of hydrodynamic loads (i.e., the horizontal force and momentum) is the largest for the case with a uniform current whereas the smallest in the decoupled models. Nevertheless, the kurtosis of the hydrodynamic load shows quite the opposite for cases with an opposing current; i.e., it is the largest in the decoupled cases whereas the smallest in the case with an opposing uniform current. It suggests that the coupled effects between surface waves and a following current lead to increased fatigue loads as the standard deviation can be a good representation of the fatigue loads. The cases for the surface elevation on the statistical deviation show evident coupled effects between waves and a following current, compared with the decoupled cases whereas the quantitative variation of the standard deviation with the spectral peak period depends on a realistic velocity profile of current.

5. Conclusions

In this paper, the coupled effects of surface gravity waves and a subsurface current in coastal waters have been examined on their exerted loading on a bottom fixed vertical slender structure. This paper firstly extends the potential flow theory to a novel semi-analytical framework which allows for rotational flow motions induced by surface gravity waves atop a depth dependent current, making it considerably different from an extensive body of literature with the assumption of irrotationality, e.g., Shen et al. (2018), Zheng et al. (2020b) and Ghadirian et al. (2021). The framework, based on the Direct Integration Method (DIM) proposed by Li and Ellingsen (2019) for the shear current-modified linear dispersion relation of surface waves and the linear wave fields, is derived up to the second order in wave steepness and assumes the waves have a narrow bandwidth. Using the numerical implementations of the new framework this paper has especially examined the coupling

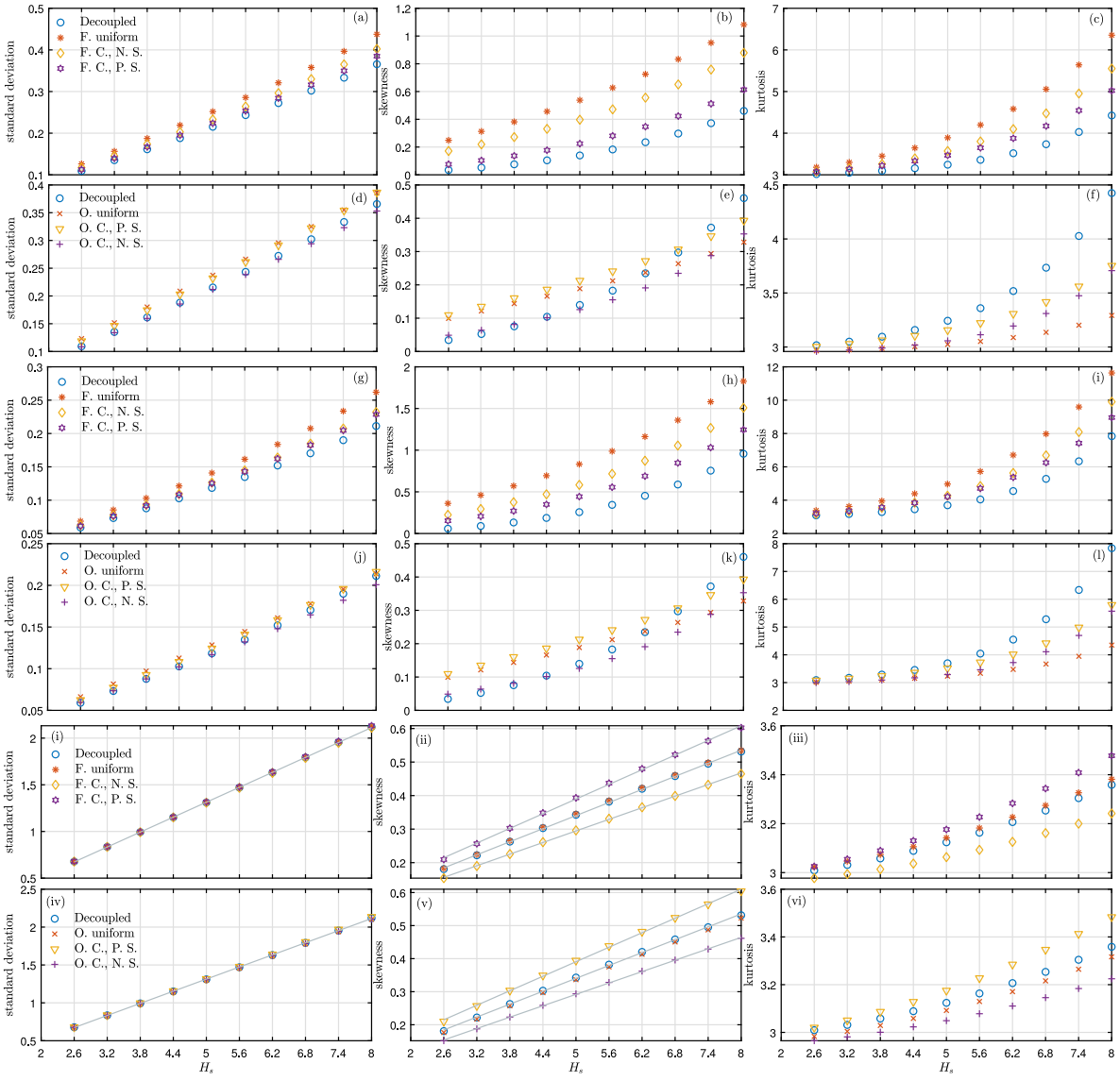

Fig. 6. Statistical moments of the horizontal force (panels a–f), moment (panels g–l), surface elevation (panels i–vi) varying with an increased significant wave height, H_s. In panels (i, ii, iv) and (v), the solid lines indicate a linear fitting of the corresponding discrete numerical predictions.

of the weak wave nonlinearity and the depth variation of a subsurface current.

The analysis of the extreme sea states indicates that the coupled effects between surface waves and a subsurface current are non-trivial and they play a more important role in the hydrodynamic loading (wave kinematics) than the surface elevation. The difference in the coupled effects on loading and surface elevation lies in their magnitude and location of the maximum of the crests. Consistent with the physical implications reported in Trulsen et al. (2020), this paper directly shows that the features of the wave kinematics are different from these of surface elevation, highlighting the need for distinguishing the proxies (e.g., the skewness and kurtosis of the surface elevation induced by random waves) to rogue waves and wave kinematics. The cases examined in this paper have especially showed that the load which occurs once every one thousand is higher by $\lesssim$50% in the coupled cases than the decoupled case while it only differs by $\lesssim$5% for the surface elevation.

This paper has also highlighted the importance of the realistic depth-dependent profile of a current in the hydrodynamic loading on offshore slender structures exposed to sea states due to waves and a subsurface current, where the angle between the wave propagation and current velocity is key. This has been demonstrated by comparing the coupled effects of waves atop a current with two different velocity profiles including a uniform and depth-varying current. Compared with the more realistic (depth-varying, following or opposing) current, we find that a uniform current following or opposing to the wave propagation tends to predict overestimated or underestimated load. A following/opposing current regardless of its depth variation leads to an increased/decreased load, compared with the decoupled case. The differences shown in the cases examined can amount to $\lesssim$25%.

Given that our theory is only second-order accurate in wave steepness and we only examined a limited number of cases, the numbers indicated in this paper are not universally accurate, but show clearly that the coupling between surface waves and a sheared current must be accounted for in the predictions of hydrodynamic loads on offshore slender structures.

CRediT authorship contribution statement

Zirui Xin: Methodology, Software, Formal analysis, Investigation, Writing – review & editing, Visualization. **Xin Li:** Supervision, Resources, Writing – review & editing, Funding acquisition. **Yan Li:** Supervision, Conceptualization, Methodology, Formal analysis, Writing – original draft, Review & editing, Resources, Funding acquisition.

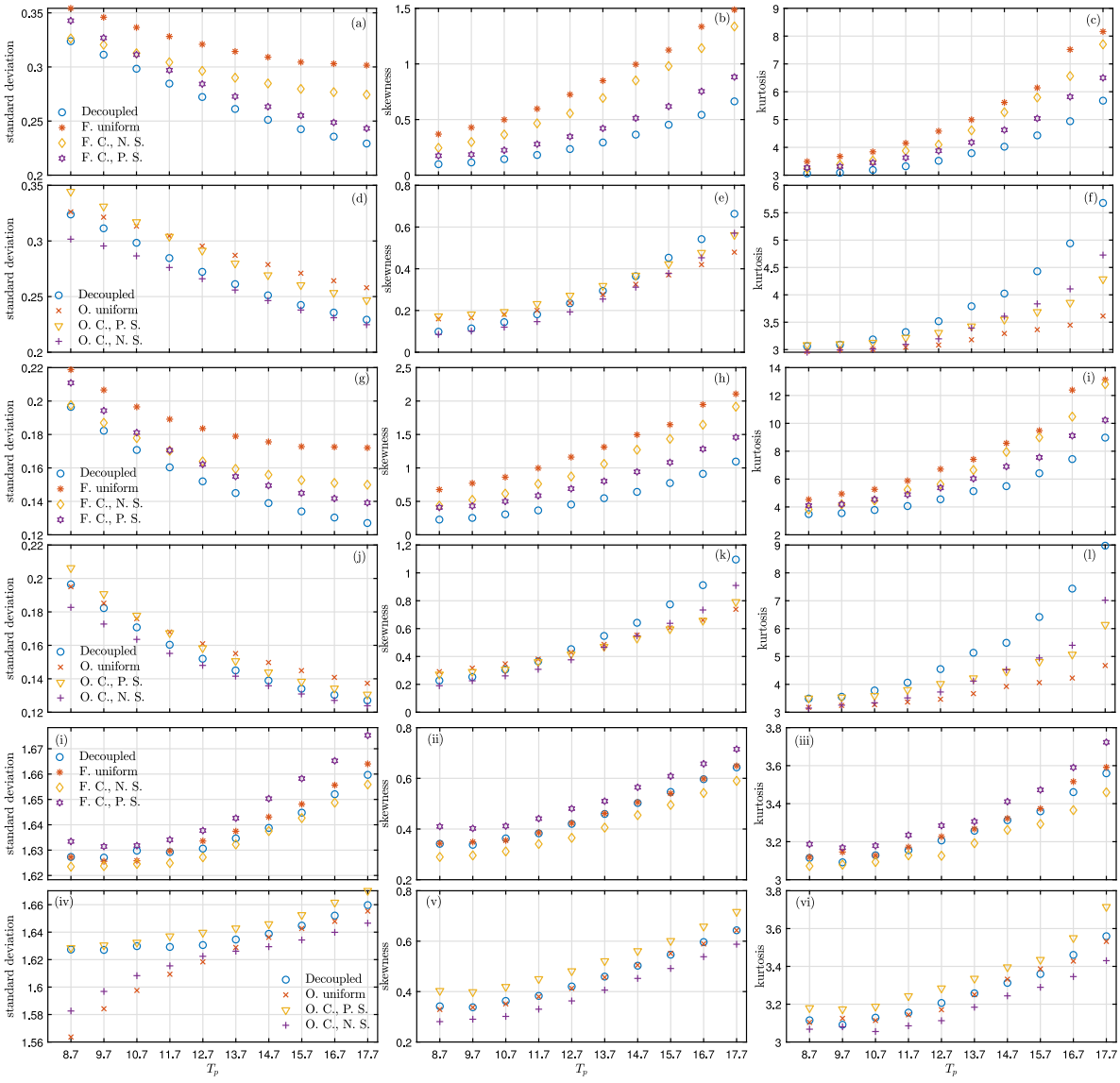

Fig. 7. Statistical moments (standard deviation, skewness, and kurtosis in the first, second, and third column, respectively) of the horizontal force (panels a–f), moment (panels g–l), surface elevation (panels i – vi) varying with an increased period of the spectral peak wave.

Declaration of competing interest

The authors declare that they have no known competing financial interests or personal relationships that could have appeared to influence the work reported in this paper.

Data availability

Data will be made available on request.

Appendix A. Validation of the numerical simulations

In this section, we validate the semi-analytical framework derived in this work which has been implemented numerically. To this end, a variety of tests were carried out in limiting cases. With analytical derivations (not shown here), we showed our solutions are in accordance with Akselsen and Ellingsen (2019) for the cases of stationary waves atop a linearly sheared current where analytical solutions are available. Two different limiting cases were selected for demonstrations based on numerical simulations. The first case aims to validate the results based on the narrowband assumption, for which available approaches are on the cases in the absence of a sheared current. We chose to compare our predictions with these based on Mei et al. (2005, §13). The case of a wave group at the linear focus was used the same as Fig. 3 for computations and the comparison is demonstrated in Fig. 8. Specifically, Fig. 8 shows the surface elevation in the different orders in wave steepness, where the agreement between the two different methods is evident. This confirms that the narrowband assumption used in our theory is as accurate as the one by Mei et al. (2005, §13) for the cases in the absence of currents.

Wave kinematics was chosen for more validation since it in principle determines the hydrodynamic loads on offshore structures. Fig. 9 shows the comparisons of the wave-induced particle velocities in the presence of currents whose profile have non-vanishing shear and curvature between laboratory observations (Swan et al., 2001), the steam function solution by Swan and James (2000), and this work. The agreements between the three different methods are evident, demonstrating that

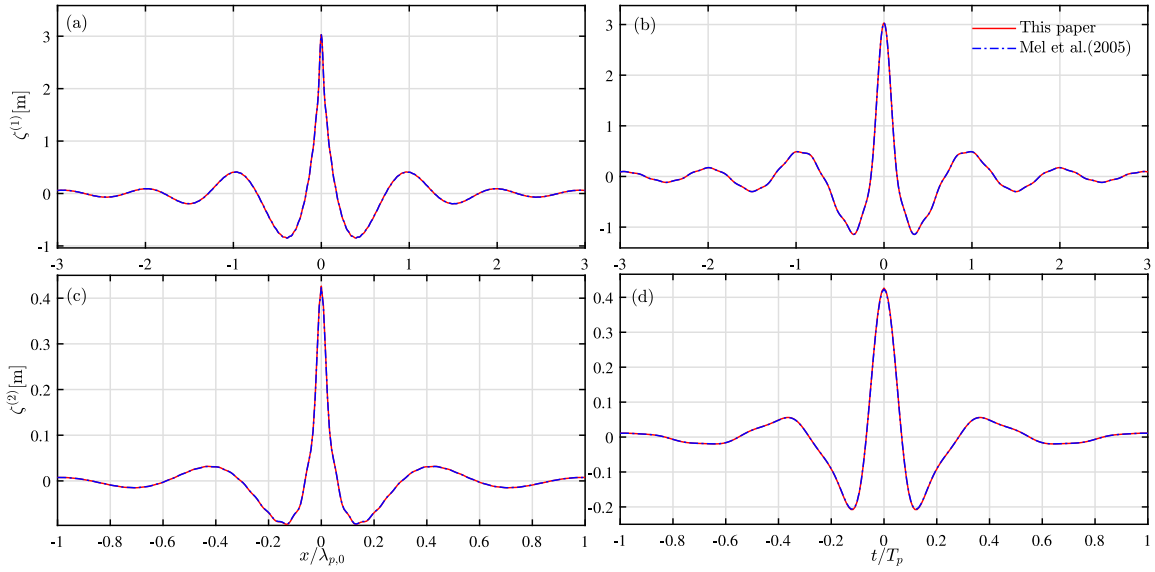

Fig. 8. Comparisons of the surface elevation in different orders in wave steepness due to a wave group in the absence of current between the predictions based on Mei et al. (2005, §13) and this work.

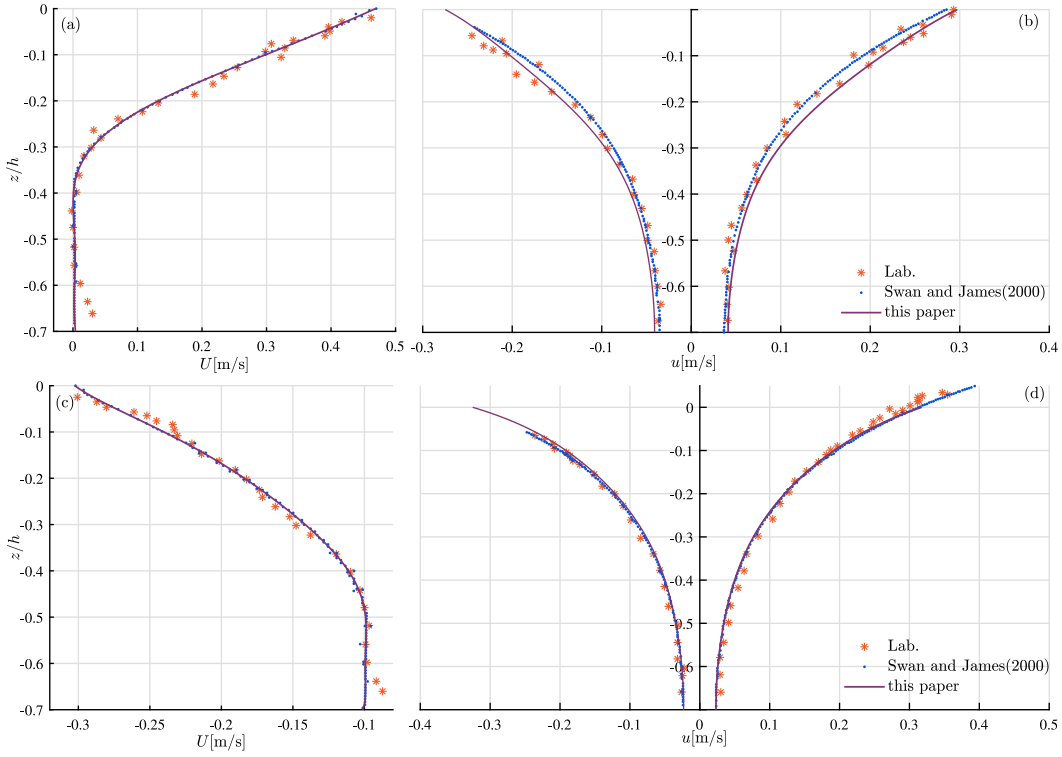

Fig. 9. The depth-dependent current profiles (panels a, c) and comparisons of the wave-induced particle velocity (panels b and d) below a wave trough (negative horizontal velocities) and crest (positive horizontal velocities) due to monochromatic waves atop a sheared current shown in the left panels between the laboratory observations (Swan et al., 2001), the predictions based on the stream function solution by Swan and James (2000), and this paper. The values for the parameters used are the same as Figs. 7 (panels a, b) and 8 (panels c, d) by Swan and James (2000).

the numerics by this paper are reliable. Minor differences can be observed between the results from this paper and that by Swan and James (2000), which might arise from the (slightly) different profile shears of the current on the still water surface and curvature of the current throughout the water column.

Appendix B. Loads by a focus wave group

In this section, Fig. 10 shows the same as Fig. 3 but case '100y' is used instead. As is clearly demonstrated by Fig. 10, similar observations

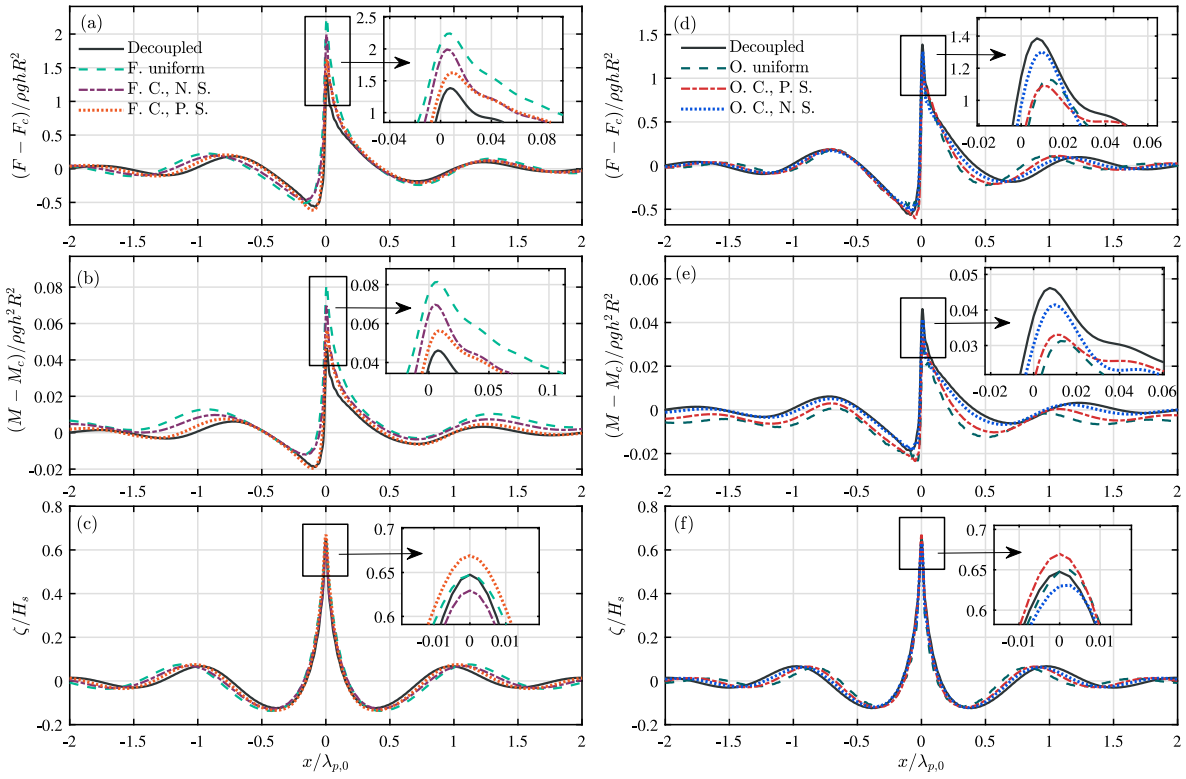

Fig. 10. Caption the same as Fig. 3 but case '100y' is used for computations.

can be seen as Fig. 3, in accordance with the conclusions drawn from the main text.

References

Akselsen, A.H., Ellingsen, S., 2019. Weakly nonlinear transient waves on a shear current: Ring waves and skewed langmuir rolls. J. Fluid Mech. 863, 114–149.

Ardhuin, F., 2017. Small-scale open ocean currents have large effects on wind wave heights. J. Geophys. Res.: Oceans (ISSN: 2169-9291) 122, 1–22.

Ardhuin, F., Marié, L., Rascle, N., Forget, P., Roland, A., 2009. Observation and estimation of Lagrangian, Stokes, and Eulerian currents induced by wind and waves at the sea surface. J. Phys. Oceanogr. 39, 2820–2838.

Benjamin, T.B., Feir, J.E., 1967. The disintegration of wave trains on deep water Part 1. Theory. J. Fluid Mech. 27 (3), 417–430.

Bredmose, H., Pegalajar-Jurado, A., 2021. Second-order monopile wave loads at linear cost. Coast. Eng. 170, 103952.

Chen, L., Basu, B., 2018. Fatigue load estimation of a spar-type floating offshore wind turbine considering wave-current interactions. Int. J. Fatigue 116, 421–428.

Chen, L., Basu, B., 2019. Wave-current interaction effects on structural responses of floating offshore wind turbines. Wind Energy 22 (2), 327–339.

DNV–GL, 2014. Environmental Conditions and Environmental Loads. Recommend Practice DNV-RP-C205.

Draycott, S., Pillai, A., Gabl, R., Stansby, P., Davey, T., 2022. An experimental assessment of the effect of current on wave buoy measurements. Coast. Eng. 174, 104114.

Dysthe, K., Krogstad, H.E., Müller, P., 2008. Oceanic rogue waves. Annu. Rev. Fluid Mech. 40, 287–310.

Ellingsen, S.Å., 2016. Oblique waves on a vertically sheared current are rotational. Eur. J. Mech. B Fluids 56, 156–160.

Ellingsen, S.Å., Li, Y., 2017. Approximate dispersion relations for waves on arbitrary shear flows. J. Geophys. Res.: Oceans 122, 9889–9905.

Faltinsen, O.M., Shen, Y., 2018. Wave and current effects on floating fish farms. J. Mar. Sci. Appl. 17 (3), 284–296.

Feng, X., Taylor, P., Dai, S., Day, A., Willden, R., Adcock, T., 2020. Experimental investigation of higher harmonic wave loads and moments on a vertical cylinder by a phase-manipulation method. Coast. Eng. 160, 103747.

Ghadirian, A., Vested, M.H., Carstensen, S., Christiensen, E.D., Bredmose, H., 2021. Wave-current interaction effects on waves and their loads on a vertical cylinder. Coast. Eng. 165, 103832.

Janssen, T., Herbers, T., 2009. Nonlinear wave statistics in a focal zone. J. Phys. Oceanogr. 39, 1948–1964.

Kirby, J.T., Chen, T.-M., 1989. Surface waves on vertically sheared flows: approximate dispersion relations. J. Geophys. Res. Oceans 94 (C1), 1013–1027.

Lawrence, C., Trulsen, K., Gramstad, O., 2021. Statistical properties of wave kinematics in long-crested irregular waves propagating over non-uniform bathymetry. Phys. Fluids 33 (4), 046601.

Li, Y., 2021. Three-dimensional surface gravity waves of a broad bandwidth on deep water. J. Fluid Mech. 926.

Li, Y., Draycott, S., Adcock, T.A.A., van den Bremer, T.S., 2021a. Surface wavepackets subject to an abrupt depth change. Part II: experimental analysis. J. Fluid Mech. 915 (A72).

Li, Y., Draycott, S., Zheng, Y., Lin, Z., Adcock, T., van den Bremer, T., 2021b. Why do rogue waves occur atop abrupt depth transitions. J. Fluid Mech. 919 (R2).

Li, Y., Ellingsen, S., 2016. Multiple resonances of a moving oscillating surface disturbance on a shear current. J. Fluid Mech. 808, 668–689.

Li, Y., Ellingsen, S.Å., 2019. A framework for modeling linear surface waves on shear currents in slowly varying waters. J. Geophys. Res. Oceans 124 (4), 2527–2545.

Li, Y., Li, X., 2021. Weakly nonlinear broadband and multi-directional surface waves on an arbitrary depth: A framework, Stokes drift, and particle trajectories. Phys. Fluids 33 (7), 076609.

Li, Z., Tang, T., Li, Y., Draycott, S., van den Bremer, T., Adcock, T.A., 2022. Wave loads on ocean infrastructure increase as a result of waves passing over abrupt depth transitions. J. Ocean Eng. Mar. Energy 9, 309–317.

Li, Y., Zheng, Y., Lin, Z., Adcock, T.A.A., van den Bremer, T.S., 2021c. Surface wavepackets subject to an abrupt depth change. Part I: second-order theory. J. Fluid Mech. 915 (A71).

Mei, C.C., Stiassnie, M., Yue, D.K.P., 2005. Theory and Applications of Ocean Surface Waves: Nonlinear Aspects, Vol. 23. World scientific.

Morison, J., 1953. The Force Distribution Exerted by Surface Waves on Piles. Technical Report, CALIFORNIA UNIV BERKELEY WAVE RESEARCH LAB.

Onorato, M., Proment, D., Toffoli, A., 2011. Triggering rogue waves in opposing currents. Phys. Rev. Lett. 107 (184502).

Onorato, M., Residori, S., Bortolozzo, U., Montina, A., Arecchi, F.T., 2013. Rogue waves and their generating mechanisms in different physical contexts. Phys. Rep. 528, 47–89.

Peregrine, D.H., 1976. Interaction of water waves and currents. Adv. Appl. Mech. 16, 9–117.

Qu, X., Li, Y., Tang, Y., Hu, Z., Zhang, P., Yin, T., 2020. Dynamic response of spar-type floating offshore wind turbine in freak wave considering the wave-current interaction effect. Appl. Ocean Res. 100, 102178.

Quinn, B., Toledo, Y., Shrira, V., 2017. Explicit wave action conservation for water waves on vertically sheared flows. Ocean Model. 112, 33–47.

Saetra, Ø., Halsne, T., Carrasco, A., Breivik, Ø., Pedersen, T., Christensen, K., 2021. Intense interactions between ocean waves and currents observed in the Lofoten Maelstrom. J. Phys. Oceanogr. 51 (11), 3461–3476.

Santo, H., Taylor, P., Day, A., Nixon, E., Choo, Y., 2018. Blockage and relative velocity Morison forces on a dynamically-responding jacket in large waves and current. J. Fluids Struct. 81, 161–178.

Sarpkaya, T., 2004. A critical review of the intrinsic nature of vortex-induced vibrations. J. Fluids Struct. 19 (4), 389–447.

Shao, Y.L., Faltinsen, O.M., 2014. Fully-nonlinear wave-current-body interaction analysis by a harmonic polynomial cell method. J. Offshore Mech. Arct. Eng. 136 (3).

Shen, Y., Greco, M., Faltinsen, O.M., Nygaard, I., 2018. Numerical and experimental investigations on mooring loads of a marine fish farm in waves and current. J. Fluids Struct. 79, 115–136.

Shrira, V.I., Slunyaev, A.V., 2014a. Nonlinear dynamics of trapped waves on jet currents and rogue waves. Phys. Rev. E 89 (4), 041002(R).

Shrira, V.I., Slunyaev, A.V., 2014b. Trapped waves on jet currents: asymptotic modal approach. J. Fluid Mech. 738, 65–104.

Stewart, R.H., Joy, J.W., 1974. HF radio measurements of surface currents. Deep-Sea Res. Oceanogr. Abstr. 21 (12), 1039–1049.

Sumer, B.M., Fredse, J., 2006. Hydrodynamics around Cylindrical Structures. WORLD SCIENTIFIC.

Swan, C., Cummins, I., James, R., 2001. An experimental study of two-dimensional surface water waves propagating on depth-varying currents. Part 1. Regular waves. J. Fluid Mech. 428, 273–304.

Swan, C., James, R., 2000. A simple analytical model for surface water waves on a depth-varying current. Appl. Ocean Res. 22 (6), 331–347.

Tang, T., Adcock, T., 2021. The influence of finite depth on the evolution of extreme wave statistics in numerical wave tanks. Coast. Eng. (ISSN: 0378-3839) 166, 103870.

Tayfun, M.A., 1980. Narrow-band nonlinear sea waves. J. Geophys. Res. C: Oceans 85 (C3), 1548–1552.

Trulsen, K., Raustøl, A., Jorde, S., Bæverfjord Rye, L., 2020. Extreme wave statistics of long-crested irregular waves over a shoal. J. Fluid Mech. 882.

Trulsen, K., Zeng, H.M., Gramstad, O., 2012. Laboratory evidence of freak waves provoked by non-uniform bathymetry. Phys. Fluids 24 (9), 097101.

Tucker, M., Challenor, P., Carter, D., 1984. Numerical simulation of a random sea: a common error and its effect upon wave group statistics. Appl. Ocean Res. 6.

Wang, J., Li, M., Liu, Y., Zhang, H., Zou, W., Cheng, L., 2014. Safety assessment of shipping routes in the South China Sea based on the fuzzy analytic hierarchy process. Saf. Sci. 62, 46–57.

White, B., Fornberg, B., 1998. On the chance of freak waves at sea. J. Fluid Mech. 335, 113–138.

Whittaker, C., Raby, A., Fitzgerald, C., Taylor, P., 2016. The average shape of large waves in the coastal zone. Coast. Eng. 114, 253–264.

Yang, J., He, Y., Zhao, Y., Shao, Y., et al., 2020. Current effect on the hydrodynamic responses of spar type floating offshore wind turbine. In: The 30th ISOPE. pp. 398–405.

Zhang, J., Ma, Y., Tan, T., Dong, G., Benoit, M., 2022. Enhanced extreme wave statistics of irregular waves due to accelerating following current over a submerged bar. J. Fluid Mech. 954.

Zheng, Z., Chen, J., Liang, H., Zhao, Y., Shao, Y., 2020b. Hydrodynamic responses of a 6 MW spar-type floating offshore wind turbine in regular waves and uniform current. Fluids 5 (4), 187.

Zheng, Z., Li, Y., Ellingsen, S.Å., 2023. Statistics of weakly nonlinear waves on currents with strong vertical shear. Phys. Rev. Fluids 8 (1), 014801.

Zheng, Y., Lin, Z., Li, Y., Adcock, T., Li, Y., van den Bremer, T., 2020a. Fully nonlinear simulations of extreme waves provoked by strong depth transitions: the effect of slope. Phys. Rev. Fluids 5, 064804.

Zippel, S., Thomson, J., 2017. Surface wave breaking over sheared currents: Observations from the Mouth of the Columbia River. J. Geophys. Res.: Oceans 122, 3311–3328.